Characterization of Ceramic Foam Filters Used for Liquid Metal Filtration

MARK WILLIAM KENNEDY, KEXU ZHANG, ROBERT FRITZSCH, SHAHID AKHTAR, JON ARNE BAKKEN, and RAGNHILD E. AUNE

In the current study, the morphology including tortuosity, and the permeability of 50-mm thick commercially available 30, 40, 50, and 80 pores per inch (PPI) alumina ceramic foam filters (CFFs) have been investigated. Measurements have been taken of cell (pore), window, and strut sizes, porosity, tortuosity, and liquid permeability. Water velocities from ~0.015 to 0.77 m/s have been used to derive both first-order (Darcy) and second-order (Non-Darcy) terms for being used with the Forchheimer equation. Measurements were made using 49-mm "straight through" and 101-mm diameter "expanding flow field" designs. Results from the two designs are compared with calculations made using COMSOL 4.2a® 2D axial symmetric finite element modeling (FEM), as a function of velocity and filter PPI. Permeability results are correlated using directly measurable parameters and compared with the previously published results. Development of improved wall sealing (49 mm) and elimination of wall effects (101 mm) have led to a high level of agreement between experimental, analytic, and FEM methods (±0 to 7 pct on predicted pressure drop) for both types of experiments. Tortuosity has been determined by two inductive methods, one using cold-solidified samples at 60 kHz and the other using liquid metal at 50 Hz, giving comparable results.

I. INTRODUCTION

CERAMIC foam filters (CFFs) have been used commercially in the aluminum foundry industry for more than four decades.[1] CFFs are industrially applied to remove small (<50 μm) solid inclusions (*e.g.*, oxides—Al_2O_3, spinels—$MgO \cdot Al_2O_3$, or carbides—SiC, Al_4C_3) and large oxide films, primarily for the production of premium quality aluminum products.

A research effort has been recently undertaken with the objective of using electromagnetic fields to achieve improved purification of liquid aluminum using commercial CFFs (30–80 PPI).[2,3] It was found in the current study that the vertical gradient in the Lorentz forces

MARK WILLIAM KENNEDY, Ph.D. Candidate, is with the Department of Material Science and Engineering, Norwegian University of Science and Technology (NTNU), 7491, Trondheim, Norway and is now Chief Technology Officer, with the Proval Partners S.A., 1004, Lausanne, Switz. Contact e-mail: m.kennedy@provalp.com KEXU ZHANG, formerly Masters Student, Department of Material Science and Engineering, Norwegian University of Science and Technology (NTNU), and is now Product Engineer, with the Wartsila Norway A.S., 5420, Rubbestadneset, Norway. ROBERT FRITZSCH, Ph.D. Candidate, and JON ARNE BAKKEN, Professor Emeritus, are with the Department of Material Science and Engineering, Norwegian University of Science and Technology (NTNU). SHAHID AKHTAR, Technical Manager (Quality), is with the Wire Rod Cast House, Hydro Aluminium, Karmøy, N-4265 Håvik, Norway. RAGNHILD E. AUNE, Professor, is with the Department of Material Science and Engineering, Norwegian University of Science and Technology (NTNU) and also with the Department of Material Science and Engineering, Royal Institute of Technology (KTH), 10044, Stockholm, Sweden.

$(\vec{J} \times \vec{B})$ induced strong movements in the liquid metal. Based on preliminary finite element magneto-hydro-dynamic (MHD) modeling and experimental observation of liquid movement within the equipment, velocities of up to 0.2 m/s are anticipated to exist within the filter elements. This velocity is approximately one order of magnitude higher than typical casting velocity for these types of commercial filters[4] and indicates that MHD dominates the flow field development. The modified filtration process can therefore not be understood, without first comprehending the impact of the Lorentz "driving" forces interacting with the resistance to flow produced by the permeability of the porous media, at these unusually high velocities.

The transition of pressure drop from first- to second-order behaviors for 65 and 80 PPI CFFs using water has been reported to be in the range from 0.01 to 0.015 m/s and to be beyond 0.015 m/s for 40 and 50 PPI filters.[5] In order to model MHD more accurately using finite element modeling (FEM) at high velocity of liquid, it was necessary to obtain both first-order (Darcy) and second-order (Non-Darcy) terms for use with the Forchheimer equation[6]:

$$\frac{\Delta P}{L} = \frac{\mu}{k_1} V_s + \frac{\rho}{k_2} V_s^2 \qquad [1]$$

where ΔP is pressure drop (Pa), L is the filter thickness (m), V_s is the fluid superficial velocity (m/s), μ is the fluid dynamic viscosity (Pa s), ρ is the fluid density (kg/m³), and k_1 (m²) and k_2 (m) are the empirical constants called the Darcian and non-Darcian permeability coefficients, respectively. Equation [1] represents the sum of viscous (first term) and kinetic energy losses (second term).

Permeability experiments were therefore conducted using water with commercial alumina CFFs of 30, 40, 50, and 80 PPI. In order to understand and correlate the obtained results, it was necessary to simultaneously study the morphology of the filters including cell (pore), window and strut sizes, porosity, and tortuosity.

II. THEORY

Permeability is an important parameter for the characterization of CFFs, since it is required to predict the flow rate obtainable for an imposed pressure gradient (*e.g.*, the casting rate for a given metal head and filter area) or to be able to predict the pressure drop (and therefore the required head or elevation change) necessary to achieve a specific flow rate for a fixed filter area (as in the design of a casting line and filter bowl). The correlation between flow and pressure drops can be obtained empirically by fitting experimental data as per Eq. [1] or by prediction using "easily" the measured physical properties such as porosity, ε (unitless), characteristic porous media dimensions, and the known liquid properties. The Ergun equation is often applied to predict the pressure drop in beds of solids[7]:

$$\frac{\Delta P}{L} = 150 \frac{(1-\varepsilon)^2}{\varepsilon^3} \frac{\mu V_s}{d_p^2} + 1.75 \frac{(1-\varepsilon)}{\varepsilon^3} \frac{\rho V_s^2}{d_p} \qquad [2]$$

where d_p is the "equivalent" spherical particle diameter (m). Even "improved" versions of Eq. [2] are known to have deviations in the range of ± 50 pct, relative to actual measured packed bed pressure drops.[8]

Given that a porous solid is not a packed bed and has no clearly definable particle diameter, d_p, it is possible to apply the Ergun formula using alternately the diameters of the cell, d_c (m), window, d_w (m), or strut, d_s (m). These diameters are indicated in Figures 1 and 2(a) through (d), for the 30 through 80 PPI filters used in this study. One would expect that the estimation errors would exceed the ± 50 pct typical of the Ergun equation, unless an appropriate "diameter" could be defined.

Ergun defined the "equivalent" particle diameter of a non-spherical solid, d_p, as the diameter of the sphere having the same "outer" specific surface area per unit solid volume, S_v (m^2/m^3) of the actual material in question (internal porosity, and small projections or cavities were ignored)[7]:

$$d_p = \frac{6}{S_v} \qquad [3]$$

In Eq. [3], the nomenclature of Ergun is maintained. Some confusion may ensue when referring to the recent literature, where S_v is sometimes used to represent the surface area of solid per unit bed volume, *i.e.*, S_B. Equation [2] can be re-written using Eq. [3] as

$$\frac{\Delta P}{L} = \alpha \frac{S_v^2 (1-\varepsilon)^2 \mu V_s}{\varepsilon^3} + \beta \frac{S_v (1-\varepsilon) \rho V_s^2}{\varepsilon^3} \qquad [4]$$

where α and β are unitless empirical constants found by Ergun to be approximately 4.17 and 0.292, respectively.[9]

Richardson *et al.*[9] explored the relationship between S_v and d_w for porous ceramics and suggested applying the
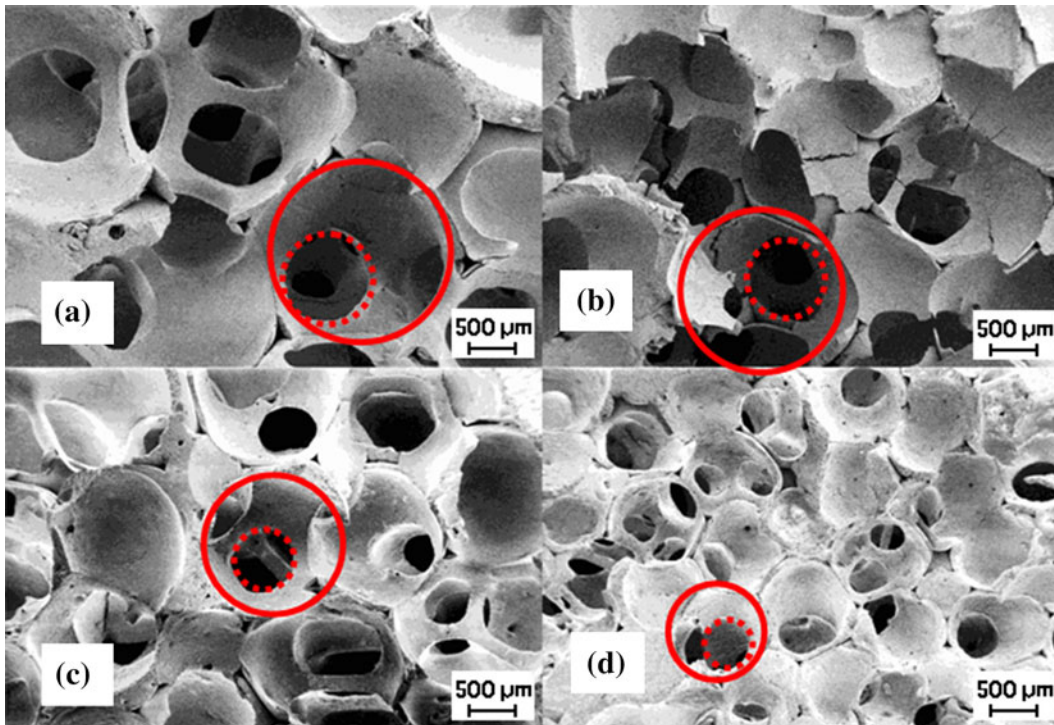

Fig. 1—Representative SEM micrographs of 30 (*a*), 40 (*b*), 50 (*c*), and 80 (*d*) PPI commercial alumina ceramic foam filters. Cell or pore sizes (d_c) are indicated by solid circles and window sizes (d_w) are indicated by dotted circles.

hydraulic diameter, d_h (m), concept. They equated the hydraulic diameter to the measured window diameter:

$$d_w = d_h = 4 \frac{\text{wetted area}}{\text{wetted perimeter}} \qquad [5]$$

Assuming idealized regular pores, i.e., all with the same hydraulic diameter, a simple geometric analysis yields

$$S_v = \frac{4\varepsilon}{d_w(1-\varepsilon)} \qquad [6]$$

Substituting Eq. [6] into Eq. [4] yields

$$\frac{\Delta P}{L} = 66.7 \frac{\mu V_s}{\varepsilon d_w^2} + 1.17 \frac{\rho V_s^2}{\varepsilon^2 d_w} \qquad [7]$$

Recently, Dietrich et al.[10,11] proposed the following equation after correlating 2500 separate experimental values from 20 authors:

$$\frac{\Delta P}{L} = 110 \frac{\mu V_s}{\varepsilon d_h^2} + 1.45 \frac{\rho V_s^2}{\varepsilon^2 d_h} \qquad [8]$$

The similarity between Eqs. [7] and [8] is obvious. If the hydraulic diameter is assumed equal to the window diameter in Eq. [8], then Eq. [8] will yield 40 through 50 pct higher pressure drops than Eq. [7].[10] As both empirical constants in Eq. [8] are larger than those in Eq. [7], it will yield higher estimated pressure drops for any velocity. Equation [8] has recently been independently shown to give excellent results using the optically determined hydraulic diameter, i.e., the equivalent circular window diameter, d_w.[12]

It should be noted that the total, ε, and open porosity, ε_o, are of very similar magnitudes, as shown in Figure 3 for an electromagnetically primed[13] 50 PPI filter filled with an A356 aluminum alloy. Some small areas of closed porosity are shown in dotted circles as typical examples of closed porosity created by the substrate used in the filter fabrication process. Grosse et al. have described the morphological characterization of CFFs
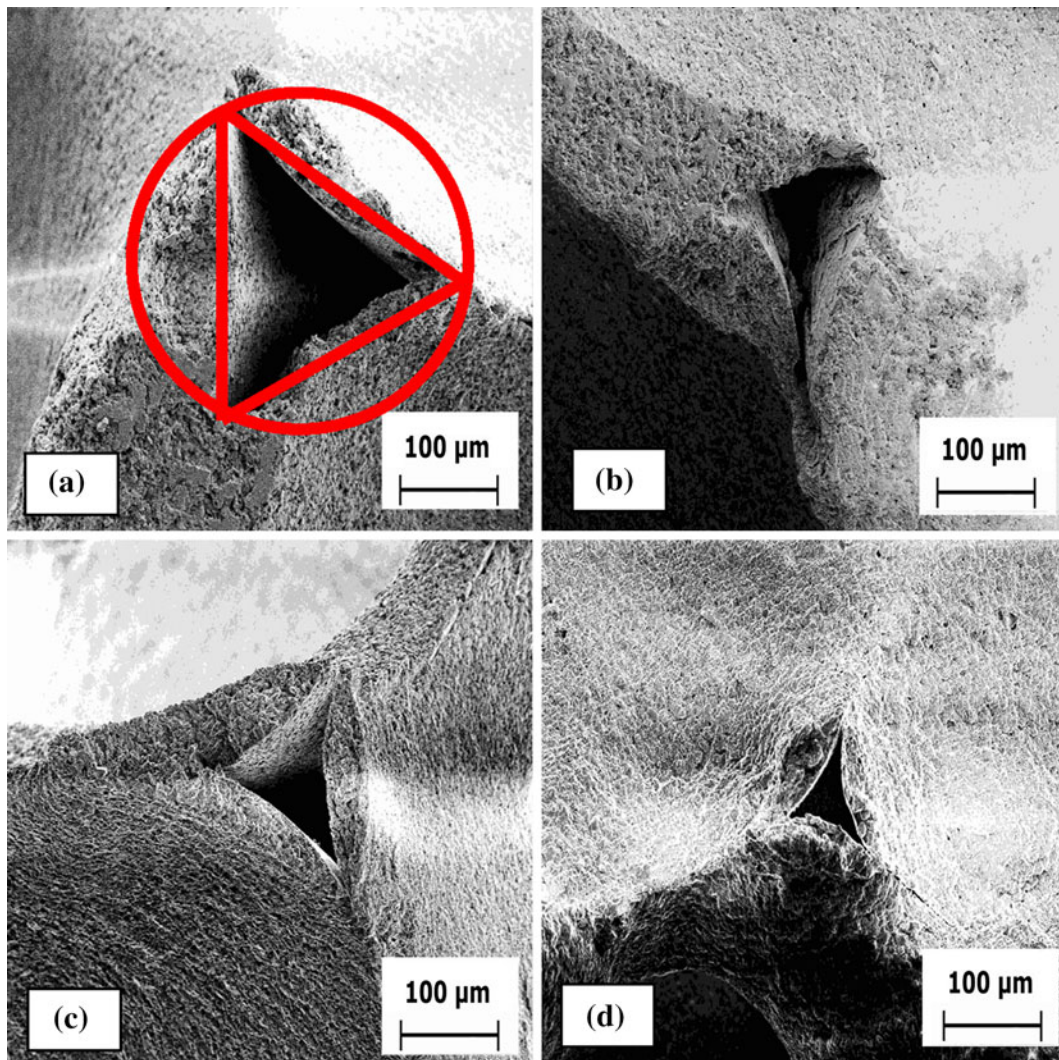

Fig. 2—Representative SEM micrographs of 30 (a), 40 (b), 50 (c), and 80 (d) PPI commercial alumina ceramic foam filters. Cell strut diameter (d_s) is indicated for the 30 PPI filter as the solid circle. The internal porosity left by the removal of the substrate is indicated as a triangle.

in detail, including the steps required to correctly determine total and open porosity (*e.g.*, using mercury at up to 4000 bar).[14,15] Grosse *et al.* found that the difference between the total and the open porosity is <5 pct of the measured value. The convention of Dietrich, *i.e.*, equality between the total and open porosities has therefore been followed in the current study.

Total porosity, ε, can be determined using the true particle density, ρ_p (kg/m^3), found using pycnometry and the measured filter mass, m_f (kg) for a known filter volume V_f (m^3), *i.e.*, the filter density, ρ_f (kg/m^3):

$$\varepsilon = 1 - \frac{m_f}{\rho_p V_f} = 1 - \frac{\rho_f}{\rho_p} \qquad [9]$$

Tortuosity, τ (unitless), is here defined as the ratio between the actual length traversed by the liquid flow, L_a (m), and the linear thickness of the filter, L (m):

$$\tau = \frac{L_a}{L} \qquad [10]$$

Tortuosity can be determined by electromagnetic induction experiments using alloys of known electrical conductivity, σ_m (Ω^{-1} m^{-1}). The actual resistance of a filter element filled with metal, as shown in Figure 3, can be compared with the known resistance of an equivalent path length of metal either liquid or solid and the tortuosity determined. The conductivity is related to the path length, area, and resistance by

$$\sigma_m = \frac{l}{a R_m} \qquad [11]$$

where σ_m is the conductivity of the metal (Ω^{-1} m^{-1}) at the measurement temperature, l is the length of the conducting path (m), a is the area of the conducting path (m^2), and R_m is the resistance of the metal along the conducting path (Ω).

Within the filter, the available conducting area is reduced by the presence of non-conducting obstructions (*e.g.*, trapped gas or solid and filter media), and the conducting path length is increased because of the tortuosity. Assuming that the filter media is the only significant obstruction, the reduced apparent electrical conductivity can be estimated as follows:

$$\sigma_f = \frac{\sigma_m \varepsilon}{\tau} \qquad [12]$$

where σ_f is the apparent electrical conductivity of the metal-impregnated filter (Ω^{-1} m^{-1}).
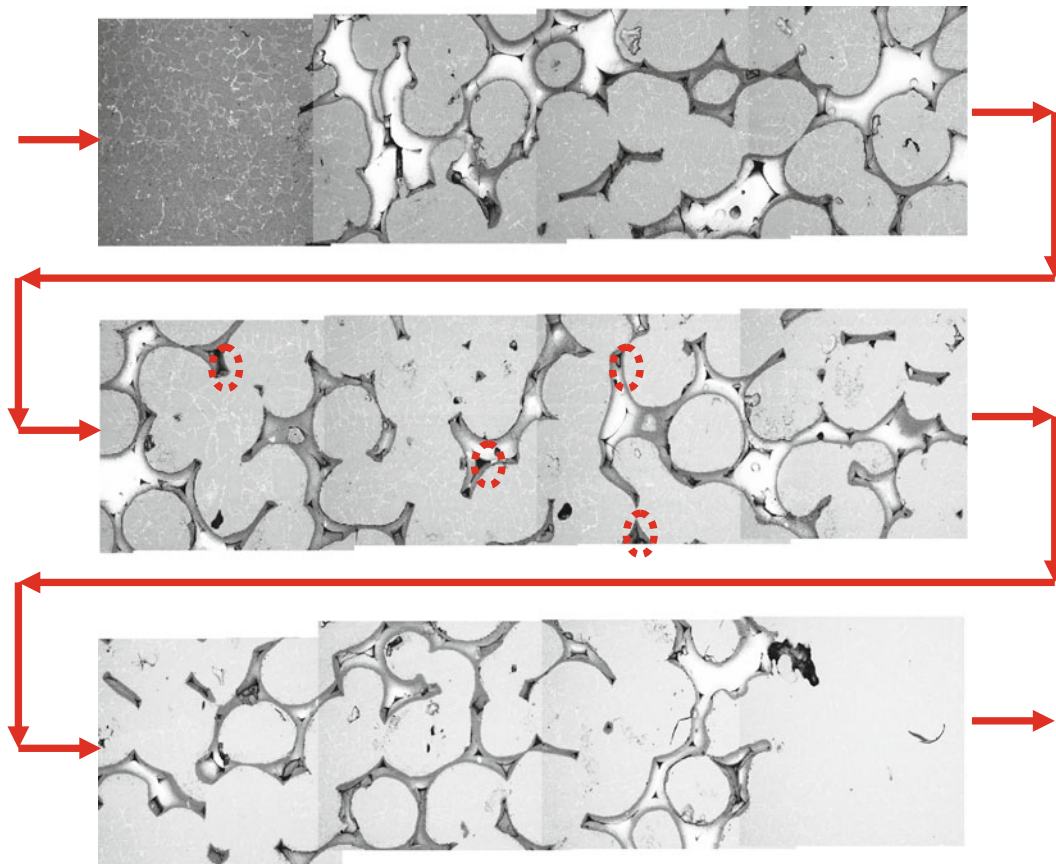

Fig. 3—Representative SEM micrographs showing a full 50-mm thickness vertical profile through a well-primed 50 PPI commercial alumina ceramic foam filter. Areas of "closed" porosity can be seen in black, some of which are highlighted by dotted circles as examples. Visual inspection confirms that nearly the entire porosity is filled with metal, *i.e.*, substantive agreement between total, ε and open porosity, ε_o.

Rearranging Eq. [12] to solve for the tortuosity yields

$$\tau = \varepsilon \frac{\sigma_m}{\sigma_f} \qquad [13]$$

III. EXPERIMENTAL

A. *Filter Characterization*

Commercial filters of 30, 40, 50, and 80 PPI where examined by a combination of light microscopy, optical scanning, and scanning electron microscope (SEM) to determine cell, d_c, window, d_w and strut, d_s dimensions. 200 counts were made for each cell and window determination, on the original, uncut surface of the 50-mm-thick alumina CFFs. 40 counts were made of the strut dimensions, which were measured at their thinnest point.

Porosities of the 101-mm filter sections used in these experiments were determined using Eq. [9] by precise measurement of the filter dimensions, calculation of the total volume, and weighing on an analytic balance. Overall precision was estimated to be ±0.2 pct porosity. The 49-mm-diameter filters used during testing were cut from the center of the 101-mm filters, and the porosities were assumed as constant. For the 30, 50, and 80 PPI filters, porosity measurements were also taken for all the commercially sized filter elements for comparison (23″, 20″, and 23″ square).

The electrical conductivity of the solid aluminum and sectioned metal-impregnated filter elements were measured using an AutoSigma 3000 inductive conductivity analyzer (General Electric Inspection Technologies, UK) to an accuracy of ±0.5 pct using a 12.7-mm-diameter 47P001 probe. The instrument was calibrated before use against certified aluminum standards of 8.64 and 60.37 pct IACS (International Annealed Copper Standard). For reference: 100 pct IACS conductivity is 58.0 MS/m,[16] and typical electrical grade aluminum (*i.e.*, "commercially" pure) has a nominal conductivity of ~61 pct IACS. Measurements were taken on metal frozen over and under the filter elements, and on both vertical and horizontal cuts through the filters. A frequency of 60 kHz was used, which resulted in electromagnetic penetration depths from ~0.3 to 0.5 mm, depending on the alloy's conductivity and filter's tortuosity. An arithmetic average on 20 through 30 readings was used to estimate the room temperature conductivity of the metal-impregnated filter. Circular induced currents (*i.e.*, eddy currents) were generated by the probe, and these represent current flow in either the r–phi axes (horizontal cut) or the r–z axes (vertical cut). It was therefore expected that readings could be different, if any anisotropy existed in the filter morphology.

The effective electrical conductivities of the filters were also determined from liquid metal electromagnetic induction experiments, using procedures described in detail elsewhere.[2,3,17] A schematic of the apparatus used is shown in Figure 4(a), and a photograph is shown in Figure 4(b). The power induced in a tight stack of three 50-mm-thick, and ~100-mm-diameter filters of 30, 40, 50, or 80 PPI was determined electrically at a known temperature (and therefore metal electrical conductivity), while being filled with "commercially pure" aluminum alloys with initial electrical conductivity from 61 to 62 pct IACS. Temperatures were logged every 100 ms by type K thermocouples located under and over the 150-mm stack of filters.

An average temperature was used to estimate the liquid metal conductivity within the filter elements, starting with the literature conductivity data for ultra pure metal, and correcting for the actual measured room temperature conductivity of the clean metal after experimentation[18]:

$$\sigma_m = \frac{IACS_m^{293K}}{24.77 \times 10^{-8} \left(1 + 0.000571 \left[T_m - 933.2\right]\right) 65} \quad [14]$$

where $IACS_m^{293K}$ is the average room temperature conductivity of the solidified metal used during the experiment (pct IACS), and T_m is the temperature of the liquid alloy under experimental conditions (K).

A 50-Hz electromagnetic field was applied along the long (z) axis of the stack of filters. This time-varying magnetic field induced circular currents along the phi-axis, through the metal-impregnated interstitial spaces of the filter elements. The induced power was determined electrically, using high accuracy instrumentation measuring changes in coil power. Power measurements were taken using a Fluke 43B power analyzer (Fluke, USA), with a resolution of 100 W. Coil current measurements were made with an i1000S inductive current probe (Fluke, USA), with an accuracy of ±1 pct and a resolution of 1A.

The effective electrical conductivity of the filter elements where then determined from the equipment geometry, the experimentally measured power (W), and the applied coil current (A), with 2D axial symmetric FEM modeling, using the commercial COMSOL 4.2a® software. Details of the validation of the modeling methods can be found elsewhere.[19,20] The FEM model had been previously shown to have ~±2 pct uncertainty in power estimation, compared with direct calorific measurements taken in solid billet heating experiments.[20] The effective conductivity was determined by adjusting the model conductivity, until the model's induced power precisely matched the measured induced power, for the given applied current. The tortuosity along the phi-axis could then be determined using Eq. [13].

The uncertainty in the tortuosity estimates then represents the sum of the uncertainty in the model (±2 pct), measured workpiece power (~±10 pct), and any error in the solid (±0.5 pct) and liquid (±5 to 10 pct) estimates of the metal conductivity. Variation of up to ±20 pct should therefore be expected on a single reading of tortuosity. Five through eight individual power readings taken once every minute were averaged to produce 1 power/tortuosity measurement. Three through eight sets of measurements (depending on the degree of thermal and electrical stability) were then
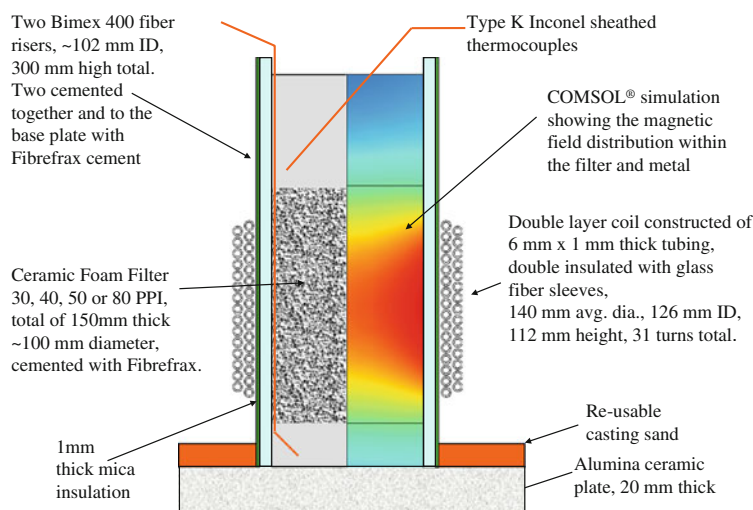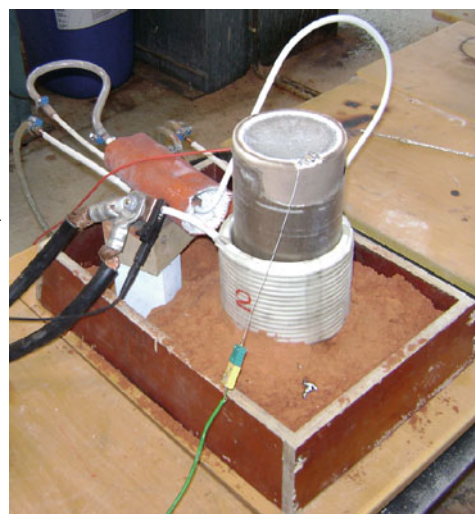
Fig. 4—Schematic of the filter tortuosity apparatus (*a*) and photograph (*b*), showing a two-layer, 31-turn (total) induction coil, operated from 371 to 734 A, using line frequency 50-Hz AC power.

individually modeled using FEM and averaged to produce the final estimate of tortuosity for each filter type.

The resulting tortuosity measurements are representative of the entire cross section of the filter, as the electromagnetic penetration depth exceeded the filter radius (50 mm), because of the low electrical conductivity of the molten metal (~10 pct of the room temperature solid metal electrical conductivity), combined with the low frequency of operation (50 Hz).

B. *Liquid Permeability: Experimental Conditions and Procedures*

The liquid permeability of 50-mm-thick commercial ceramic foam filters (CFFs) with 30, 40, 50, and 80 PPI were measured using water as the working fluid, in a temperature range from 278 K to 281 K (5 °C to 8 °C) (typical ρ_w = 999.9 kg/m^3, and μ_w = 1.3775 10^{-3} Pa s). Mass flows from about 0.05 to 2 kg/s of water were circulated through 46.4-mm ID smooth plastic piping, representing Reynolds numbers from ~1200 to 39000 and moving from laminar flow, into transitional and partially turbulent pipe flow in the inlet pipe.[21]

Eight through ten different experimental velocities were used to measure pressure drop for each filter. 101-mm nominal diameter elements were cut from the full size (20″ or 23″ square) commercial filters using diamond bores. The 49-mm diameter filter elements were cut from the center of the 101-mm filter elements. The true diameter and thickness of each filter element were measured using a micrometer, and the averages of six readings were used in the subsequent experimental analysis.

The main Plexiglas filter apparatus used in the permeability experiments is shown in Figures 5(a) and (b). The use of a transparent housing ensured that all air

was completely eliminated from the system before recording any pressure readings. Two apparatus designs where used: one for the 101-mm diameter filters, shown in Figure 5(a); and the second, for 49-mm filters, shown in Figure 5(b). The sealing arrangements were of critical importance in the design of the filter housings. In order to prevent wall effects from significantly affecting the results, it is of paramount importance to prevent the flow from bypassing the filter and moving along the walls. Therefore, in the final experimental procedure, high-viscosity silicone grease was used to smoothen the outer surface of each filter (fill the outer-most broken or cut cells), which were then wrapped in paper and pressed tightly into the holder. Upon making contact with water, swelling of the cellulose fibers provided a seal of negligible permeability. It is necessary to seal the entire side surface of the filter, as normal O-rings are unable to stop the flow from bypassing along the wall.

In the 101-mm diameter design, the impacts of "wall effects" are essentially eliminated by allowing the flow field to expand within the filter element and making the outer wall a "stagnant" region. FEM is then required to elucidate the flow field and calculate an "effective" flow diameter for use with Eq. [1], which assumes a single representative diameter. It was necessary to use soft rubber gasket materials to press into the top and bottom faces of the filter elements, to prevent horizontal flow at the inlet or outlet and provide a clearly defined "entrance/exit diameter" of 49 mm for later CFD analysis.

The pressure transducer used was a DF-2 (AEP Transducers, Italy), with measuring range from 0 to 1 bar, and equipped with an output range from 4 to 20 mA. The transducer was factory calibrated and certified to an error of <±0.04 pct of reading, over the full scale from 0 to 1 bar, using a six-point calibration. During the experiments, the current produced by the transducer at zero liquid flow velocity was determined

manually using a FLUKE 26 III, True RMS Multimeter (Fluke, USA) to a precision of 0.001 mA (6.25 Pa), using the lowest available current scale. Currents during the flow measuring periods were computer data logged at 100-mS intervals by conversion to signal range from 0 to 5 V, with a resolution of 0.001 V or 0.004 mA (*i.e.*, 25 Pa resolution). At greater than 4.1 mA, no bias could be detected between the manual and automated current readings, at the available 0.01 mA resolution (the FLUKE meter switched to a lower resolution at greater than 4.099 mA). The length between the pressure taps was 160 mm (varying ~±1 mm). One tap was located at 1.5 L/Ds up-stream and the other 0.75 L/Ds down-stream of the filter element.

The required inlet lengths to fully develop the flow regime are

Laminar[22]:

$$\frac{L_{inlet}}{d_{pipe}} \approx 0.03 Re_{pipe} \qquad [15]$$

Turbulent[23]:

$$\frac{L_{inlet}}{d_{pipe}} \approx 4.4 Re_{pipe}^{1/6} \qquad [16]$$

where L_{inlet} is the required inlet length (m) to fully develop the flow profile (*e.g.*, 99 pct centerline approach), d_{pipe} is the inside diameter of the pipe (m), and Re_{pipe} is the pipe Reynolds number (unitless).

The filter holders were used in a piping circuit containing ten 90 deg bends, with five being located before and five after the filter holder apparatus. There was a total of 8.3 m of piping in the standard "short" inlet configuration and 12.3 m in the "long" inlet configuration. In the "short" configuration, there were 22 L/Ds of straight sections of pipe before the filter housing, and in the "long" configuration, there were 65 L/Ds.

From Table I, it can be seen that except at very low or very high velocity, the "short" inlet should be adequate to achieve fully developed flow (*i.e.*, "99 pct approach"), while the "long" inlet should be adequate at all Reynolds numbers. The impact of back-to-back and out-of-phase 90° bends on the flow will be to promote turbulence even at low Reynolds numbers. Owing to the difficulty of simulating such a complex flow path (originating at a centrifugal pump), 3D fluid flow modeling was not deemed to be warranted. Various biased flow inlet conditions were tested for the "long" and "short" inlet lengths using 2D axial symmetry FEM and were found to have only second-order effects at the most. For FEM modeling, an extremely simplistic uniform inlet velocity was therefore assumed at the entrance to the pressure apparatus shown in Figures 5(a) and (b); the reasonableness of this assumption then is subject to empirical verification.

The pressure in the system was produced by a 1000 W, 0.8 bar maximum submersible pump, which was located at the bottom of a 70-cm-tall holding tank of 100-L capacity. The water flow rate was regulated using a DN 25 ball valve, located immediately at the outlet of the

Table I. Required Inlet Length to Fully Develop Flow as a Function of Pipe Reynolds Number

Velocity (m/s)	Pipe Re	L/D Inlet Laminar	L/D Inlet Turbulent	Estimated L/D Inlet
0.03	1010	30.3	N/A	30.3
0.05	1684	50.5	15.2	32.8
0.1	3368	N/A	17.0	17.0
0.2	6736	N/A	19.1	19.1
0.4	13472	N/A	21.5	21.5
0.8	26945	N/A	24.1	24.1
1	33681	N/A	25.0	25.0
1.2	40417	N/A	25.8	25.8

$d_{pipe} = 0.0464$ m, $\rho_w = 999.9$ kg/m^3, and $\mu_w = 1.3775 \times 10^{-3}$ Pa s.
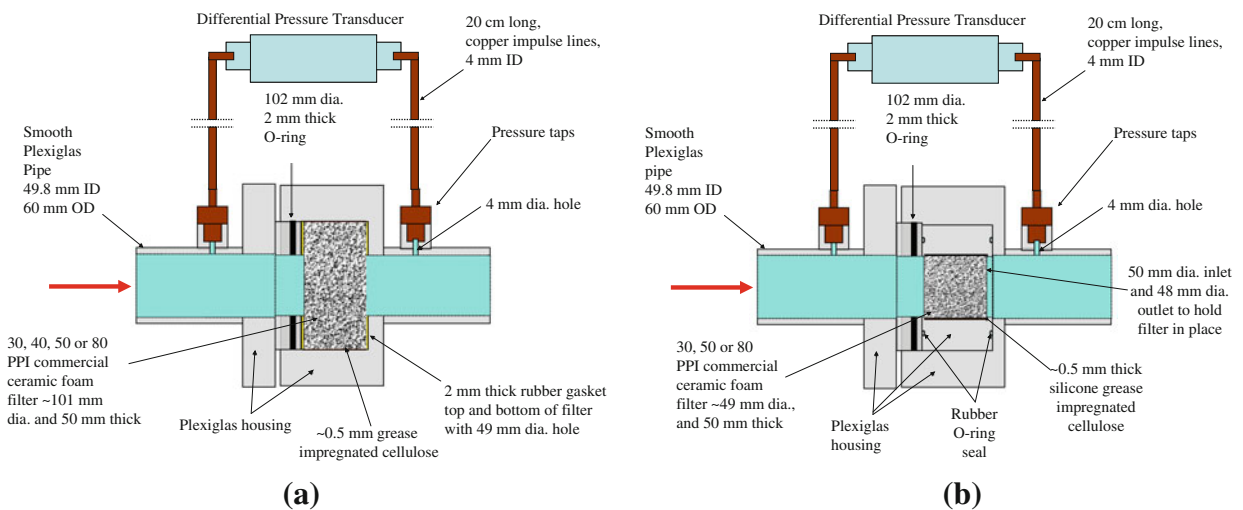

(a)

(b)

Fig. 5—Apparatus used for the 101-mm (*a*) and the 49-mm (*b*) diameters, 50-mm-thick filter experiments, both drawn approximately to scale. Fluid flow was from right to left.

pump. The flow rate was determined by accumulating mass over the measuring period in a second 100-L tank, located on a digital balance, equipped with an output range from 4 to 20 mA. The scale had a resolution of 10 g and a maximum reading of 100 kg. The zero and span of the scale were verified for accuracy at the 10-g resolution using test weights to 50 pct of full scale before use. The rate of mass gain of the measuring tank was computer data logged at 100 ms intervals. Depending on the required mass flow, from 10 to 50 kg of water was accumulated. "Sloshing" of the water in the tank (mainly at very high flows) produced noise on the weight signal that was smoothened by taking a 1-s rolling average (rolling average of 10 readings), which resulted in a maximum flow rate uncertainty of ~±0.5 pct of reading. The flow rate was found from the slope of the accumulation of mass with time and determined using least squares regression over the whole measuring period (typical $R^2 = 0.9985$). Temperatures were measured using a 1-mm-diameter Inconel-sheathed Type K thermocouple located in the holding tank, and the temperature data were also computer logged.

Eq. [1] was used with the measured pressure gradients and superficial velocities to determine the Forchheimer terms k_1 and k_2. Each estimate used the appropriate water temperature, and therefore density and viscosity, representative of the individual mass flow reading. Superficial velocity was determined using the actual measured filter diameter for the 49-mm filter elements or using the "effective" flow field diameter for the 101-mm filter elements (to be described in more detail later). Final k_1 and k_2 values are the arithmetic average of the 8 through 10 values determined for each filter element.

IV. RESULTS

A. Filter Characterization

SEM micrographs indicating the physical structures ranging from 30 to 80 PPI alumina ceramic foam filters used in this study are shown in Figures 1 and 2. The filter porosity and key dimensions are summarized in Table II. Sample porosity was calculated using Eq. [9] from the measured particle density of 3.48 ± 0.02 g/cm^3 (average of 3 readings). Overall filter porosity indicated in Table II is the average result of 2 through 4 readings on industrial 20″ or 23″ filters.

Histograms have been made of the 200 counts of window diameter, d_w as can be seen in Figures 6(a) through (d) for the 30 to 80 PPI filter types. Median

values are indicated by dotted lines. Average cell diameter, d_c, has been plotted vs. the average window diameter, d_w in Figure 7, and the results correlated according to the following equation:

$$d_c = 1.79d_w, \ R^2 = 0.988 \quad [17]$$

The linear relationship between cell and window diameters implies a simple geometric relationship, likely originating with the original substrate used during the filter fabrication process. There is an excellent agreement between the current findings and the literature values for both cell and window sizes for similar alumina CFFs.[24]

B. Filter Tortuosity Measurements

Filter tortuosity has been determined for metal-impregnated 30, 40, 50, and 80 PPI filters. Measurements have been obtained with the metal in both liquid and solid states. The metal used was "commercially" pure electrical grade aluminum, which was determined to have 61.7 ± 0.1 pct IACS conductivity (average of 10 readings) before melting. After melting, the solidified metal samples were found to have conductivities of 59.7 pct (30 PPI), 54.0 pct (40 PPI), 60.0 pct (50 PPI), and 61.0 pct (80 PPI). The hot metal experiments were conducted using the apparatus already shown in Figure 4, and detailed results can be found in Appendix Table I.

Hot liquid metal (FEM estimate) and cold-solidified filter section measurements (average, vertical, and horizontal cuts) and calculated tortuosity results (using the hot metal data) are summarized in Table III, for all four filter types. Experimental data have also been plotted in Figure 8.

Results show reasonable agreement between hot and average cold conductivity ratios, given the different equipments, temperatures, and frequencies involved in these two sets of measurements. The conductivity ratio between the metal and metal-impregnated filters for the liquid metal experiments was correlated according to the following equation:

$$\frac{\sigma_m}{\sigma_f} = 5.10 - 3.8 \times 10^3 d_w, \ R^2 = 0.981 \quad [18]$$

The variation in conductivity ratios between the horizontal or vertical cuts appeared to be random in nature. The observed variations may be the result of the

Table II. Summary of Basic Filter Physical Properties

Filter Type (PPI)	Filter Porosity (Eq. [9])	Full Filter Porosity (Eq. [9])	Cell Diameter, d_c (μm)	Window Diameter, d_w (μm)	Strut Diameter, d_s (μm)
30	0.892	0.890 ± 0.0002	1668 ± 417	961 ± 190	185 ± 41
40	0.900	N/A	1306 ± 251	698 ± 151	211 ± 46
50	0.863	0.864 ± 0.004	1132 ± 130	623 ± 120	190 ± 36
80	0.865	0.860 ± 0.004	683 ± 87	383 ± 87	119 ± 20

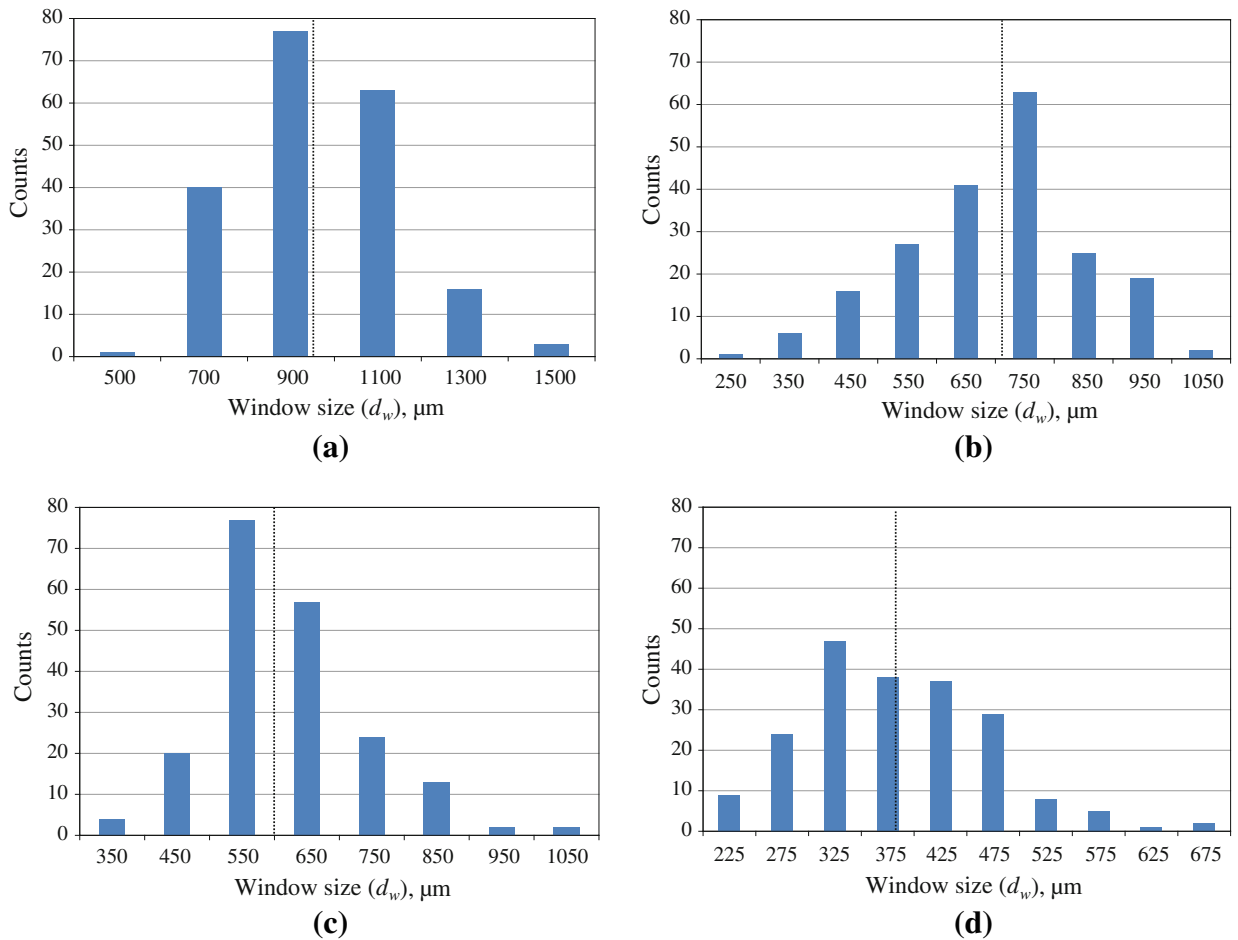One standard deviation is indicated by the ranges.

Fig. 6—Histograms of (a) 30, (b) 40, (c) 50, and (d) 80 PPI window sizes, d_w (μm). Median values are marked with dotted lines.
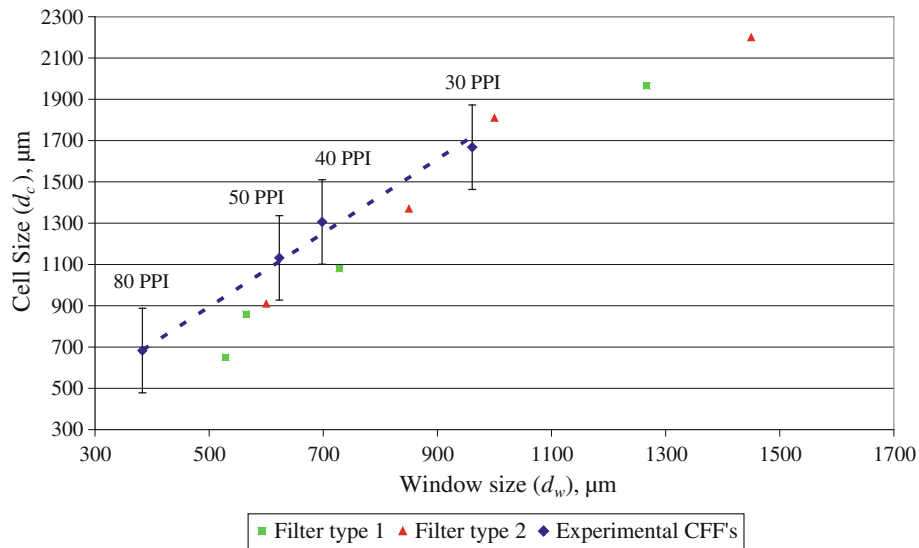

Fig. 7—Commercial ceramic foam filter cell size, d_c vs. window size, d_w (μm), and comparison with the literature data.[24] One "standard error" is indicated by the error bars.

random location of the sections through the pore structure of the filter elements and the low electromagnetic penetration depth of the high-frequency cold method, which is less than one cell diameter.

Relatively very few measured values have been published previously for ceramic foam tortuosities. Moreia *et al.* measured tortuosity values using an ionic conduction method equivalent to the induction method

described here. Their values for ceramic foams of 8, 20, and 45 PPI were 1.68, 1.71, and 1.84, respectively.[25] Diedericks *et al.* have theoretically studied tortuosity in some detail, proposing a value of ~1.45 at $\varepsilon = 0.88$, for "foam-like" materials.[26] Methods, using water and ionic solutes, will likely underestimate the true filter tortuosity, because of penetration of the water and ions into the micro and nano-porosity of the filter structure itself. Liquid metal

Table III.   Summary of Key Tortuosity Experimental Results

Filter Type (PPI)	Filter Porosity (Eq. [9])	Filter Tortuosity (Eq. [13])	FEM Estimate of Conductivity Ratio (σ_m/σ_f)	Cold Average Conductivity Ratio (σ_m/σ_f)	Cold Vertical Conductivity Ratio (σ_m/σ_f)	Cold Horizontal Conductivity Ratio (σ_m/σ_f)
30	0.892	1.30	1.46 ± 0.06	1.70	1.64	1.77
40	0.900	2.29	2.54 ± 0.18	2.15	2.27	2.02
50	0.863	2.19	2.54 ± 0.12	2.70	2.34	3.05
80	0.865	3.20	3.70 ± 0.06	2.79	2.91	2.66
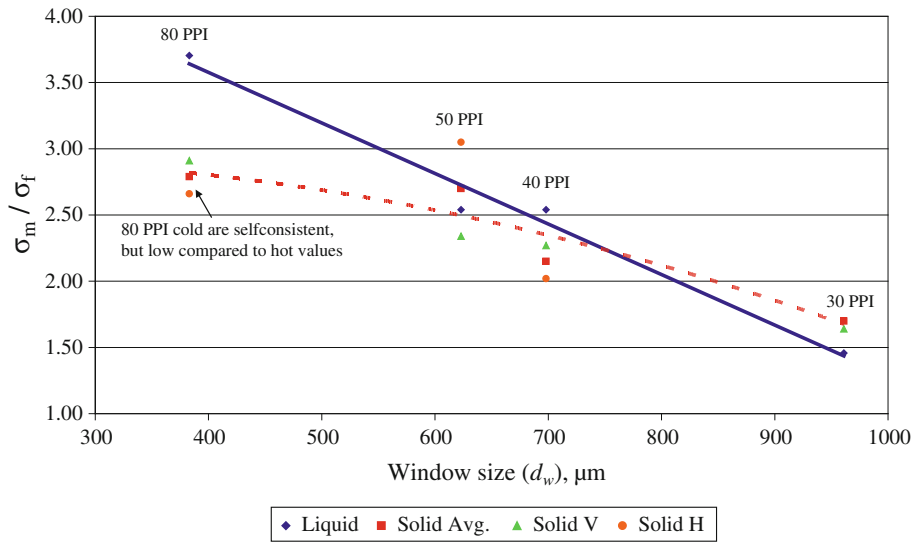
Fig. 8—Conductivity ratio of metal, σ_m and metal-impregnated filter, σ_f *vs.* window size, d_w (μm). Comparison between liquid metal values fitted to experimental data using FEM and average, vertical, and horizontally cut solid filter sections (cold readings).
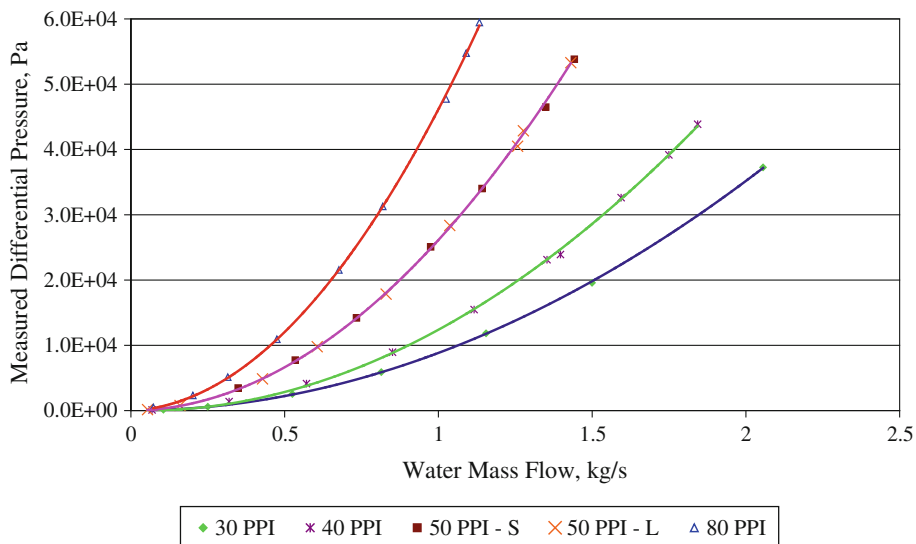

Fig. 9—Ceramic foam filter pressure drop measurements (Pa) as a function of water mass flow (kg/s) for the 101-mm "expanding flow field" filter design.
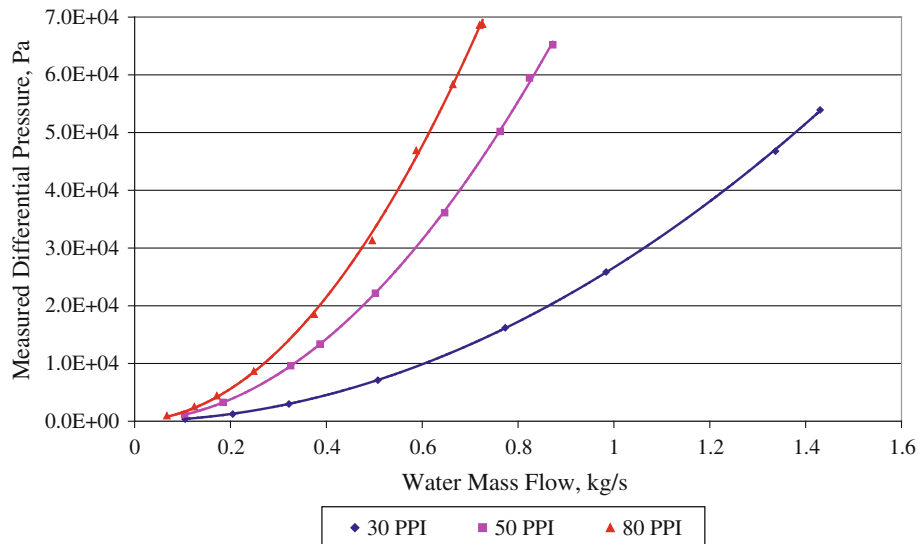
Fig. 10—Ceramic foam filter pressure drop measurements (Pa) as a function of water mass flow (kg/s) for the 49-mm "straight through" filter design.

Table IV.   Empirical Coefficients for Eq. [19]

Filter Type (PPI)	Filter Diameter (mm)	A (Eq. [19])	B (Eq. [19])	R^2 (Eq. [19])
30	101	8754	83.2	0.9999
40	101	13362	−974.4	0.9996
50	101	25703	428.6	0.9997
80	101	44142	2017.1	0.9998
30	49	25480	1131.9	1.0000
50	49	83965	1771.7	0.9998
80	49	129032	1960.1	0.9994

poorly wets the surface of the ceramic, and in the absence of intense pressure (*e.g.*, 4000 bar for mercury) will not penetrate the micro porosity.

C. *Filter Permeability Measurements, Analytic and FEM Modeling*

Permeability measurements were performed using 101- and 49-mm-diameter filters as shown in Figures 5(a) and (b). Results for these experiments are summarized in Figures 9 and 10. Results are nearly perfectly described by second-order empirical equations of the following form:

$$\text{Filter Pressure Drop (Pa)} = A\dot{m}^2 + B\dot{m} \quad [19]$$

where A and B are empirical constants, and $\dot{m}$ is the measured mass flow rate of water (kg/s). Values for the coefficients A and B are summarized in Table IV.

The experiments conducted using the 101-mm filters allowed the flow field within the filter element to expand, virtually negating wall effects; however, these experiments did not have a defined flow area, and therefore had no definable velocity for use with Eq. [1]. In order to determine the Forchheimer k_1 and k_2 terms using the 101-mm filters, it was necessary to use computational fluid dynamics (CFD) to solve for the flow field. An iterative procedure was applied as described in Figure 11. An "effective" flow field diameter was initially assumed for use with Eq. [1], the resulting k_1 and k_2 terms were then used with the CFD model, and the pressure gradients determined. If the results were in error, then a new "effective" diameter was assumed, and the procedure repeated until convergence was achieved. Example flow fields for the 101- and 49-mm diameter filter apparatus at 280 K (7 °C) and 0.5 m/s inlet water velocity are shown in Figures 12(a) and (b), respectively.

Results for the Forchheimer k_1 and k_2 terms for the 49- and 101-mm filters are summarized in Table V. More detailed results are given in Appendix Table II. The FEM-estimated k_1 and k_2 parameters for the "expanding flow field" 101-mm diameter experiments do not deviate by more than 16 pct from the directly measured "straight through" results for either k_1 or k_2.

Excellent agreement was found between the measured pressure gradients and those predicted using 2D axial symmetric FEM or analytic Eq. [1]. Deviations were in the range of ±0 to 7 pct, as plotted in Figures 13 and 14, against the 1:1 diagonal. This level of agreement can be taken as empirical confirmation of the adequateness of the uniform inlet velocity profile assumed in the FEM modeling and the use of the "effective" diameter for the analytic modeling using Eq. [1] of the "expanding flow field" 101-mm filters.

Important confirmation is also evidenced by the lack of variation of the measured pressure gradient between experiments conducted using 50 PPI, 101-mm diameter filters with the "long" and "short" inlet length configurations and the equivalent 49-mm filter, with the "short" inlet configuration, as shown in Figure 15. This figure verifies that inlet length and variation of the inlet
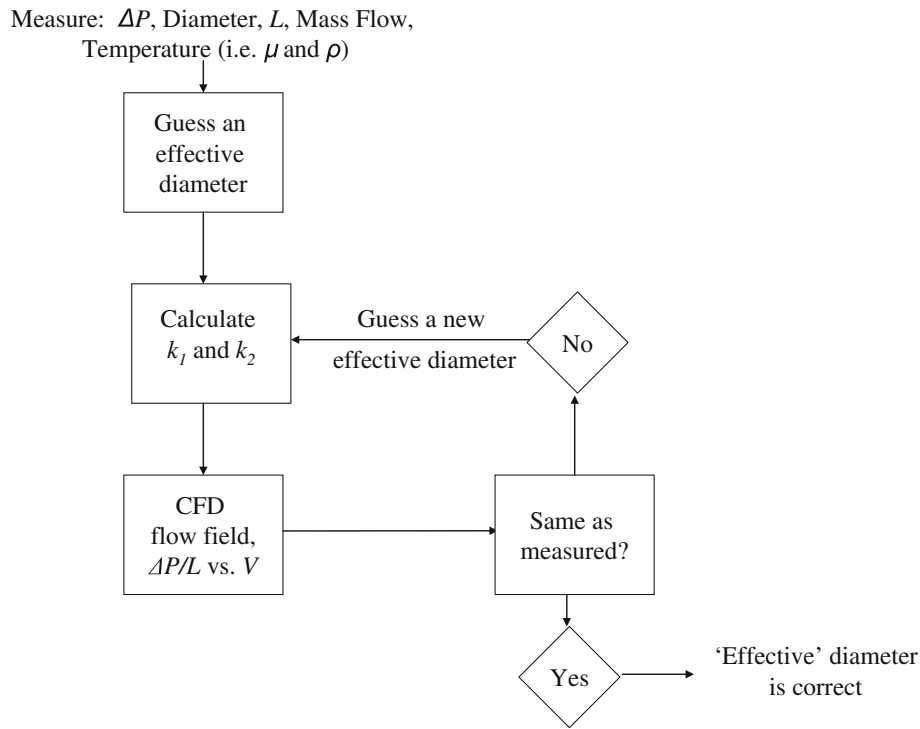
Fig. 11—FEM CFD procedure applied to the 101-mm experimental results to determine the Forchheimer, Eq. [1], parameters k_1 and k_2.

condition from laminar to turbulent pipe flow over the range of flow conditions should not have resulted in significant (*i.e.*, measurable) biases to the results.

V. DISCUSSION ON PERMEABILITY MEASUREMENTS

A. *Forchheimer Eq. [1] Coefficients, k_1 and k_2*

Using the apparatus in this study, the pressure resolution during flow was better than 62.5 Pa, *i.e.*, the 0.01 mA manual verification of automated readings (which had a theoretical resolution of 25 Pa), or a gradient uncertainty of ~±625 Pa/m depending on the sample. 625 Pa/m represented >5 pct uncertainty at flow rates in the range from 0.03 to 0.08 m/s, depending on the filter PPI. It has previously been reported that the transition to second-order behavior occurs at <0.02 m/s for 65 and 80 PPI filters similar to those used in these experiments.[5] With the limitations of the apparatus, it was therefore necessary to determine both k_1 and k_2 from flow conditions, where both terms were simultaneously significant, *i.e.*, it was not possible to operate in a purely "Darcy" regime.

In order to derive the Forchheimer coefficients in Table V, three procedures were explored:

(a) An "automated" second-order regression, with a zero intercept, using Excel 2003/2010.
(b) Ergun *et al.*'s procedure of dividing Eq. [1] by the velocity and performing a linear regression.[27]

(c) An iterative procedure to first guess k_1 and then correlate the remainder for k_2 using an exponential regression.

It should be noted that the values for the coefficients A and B summarized in Table IV for Excel 2nd-order correlations of the data can be converted to the Forchheimer coefficients through simple mathematical manipulation. This clearly makes the negative coefficient (B) for the 40 PPI physically meaningless, even when $R^2 = 0.9996$.

No physically meaningful correlations could be performed on the values of k_1 and k_2 found using Excel, *e.g.*, comparison with total porosity or window size. Better results were obtained following the recommended method of Ergun. The most physically meaningful results (*i.e.*, those with a clear trend) were obtained following the third procedure, where k_1 was initially guessed, the first-order component of Eq. [1] subtracted from the total and an exponential regression performed on the remainder. When the exponent on the velocity became 2.00000, the procedure was deemed converged. These are the values of k_1 and k_2, previously presented in Table V. k_1 and k_2 obtained by all the three methods are summarized in Appendix Table II for reference.

The third procedure appeared to prevent experimental variance from appearing disproportionately in the first-order k_1 term. Very small percentage errors in measured pressure at high velocity, represent very large errors when compared with the magnitude of pressure measured at low velocity, given the two orders change in magnitude with velocity, *i.e.*, "small" errors at high velocity can produce large changes in the estimated values for k_1.

The k_1 and k_2 values from Table V have been plotted in Figure 16 as functions of the window diameter d_w, and more specifically the window area, $\frac{\pi d_w^2}{4}$. Empirical correlations have been developed for k_1 (m^2) and k_2 (m) as functions of the window diameter d_w (m):

$$k_1 = \frac{6.71 \times 10^{-2} \pi d_w^2}{4}, \ R^2 = 0.974 \quad [20]$$

$$k_2 = \frac{7.27 \times 10^2 \pi d_w^2}{4}, \ R^2 = 0.960 \quad [21]$$

From Figure 16 and Eqs. [20] and [21], it is concluded that from 30 to 80 PPI filters tested in these experiments behave much more like a series of "orifices," than they do a series of struts as is assumed in simple cubic cell[28,29] or more complex dodecahedron[30] and tetrakaidecahedron[9,31,32] models. An examination of Figure 1 would seem to support the concept of "orifices," given the high percentage of closed windows, particularly at higher PPIs. A simple strut model would not appear to be valid for the ceramic foam filters used in this study.

B. Development of the Experimental Method

Concern with regard to bypassing of the flow around the filters and down the wall of the apparatus was the primary consideration in the design of the filter holder apparatus, as explained in the experimental section. The previous literature provided little guidance on the detailed design of the filter holder or how to produce functional wall sealing arrangements.

A series of incremental improvements were therefore necessary to arrive at the final procedure. The initial "expanding flow field" 101-mm apparatus was operated without wall sealing, and this was found relatively adequate, except at the highest velocity/pressure drops and the "tightest" 80 PPI filters. High flow and tight filters created large driving forces for bypassing.

The use of the "straight through" 49-mm apparatus necessitated the development of adequate wall sealing. High viscosity silicone was initially used alone, but visual observation through the Plexiglas housing showed that the sealant was forced out of the channel at the wall for 50 and 80 PPI filters, particularly during operation at high velocity and high pressure. The loss of seal was verified experimentally by repeating measurements and comparing with the previously "well-sealed" results as
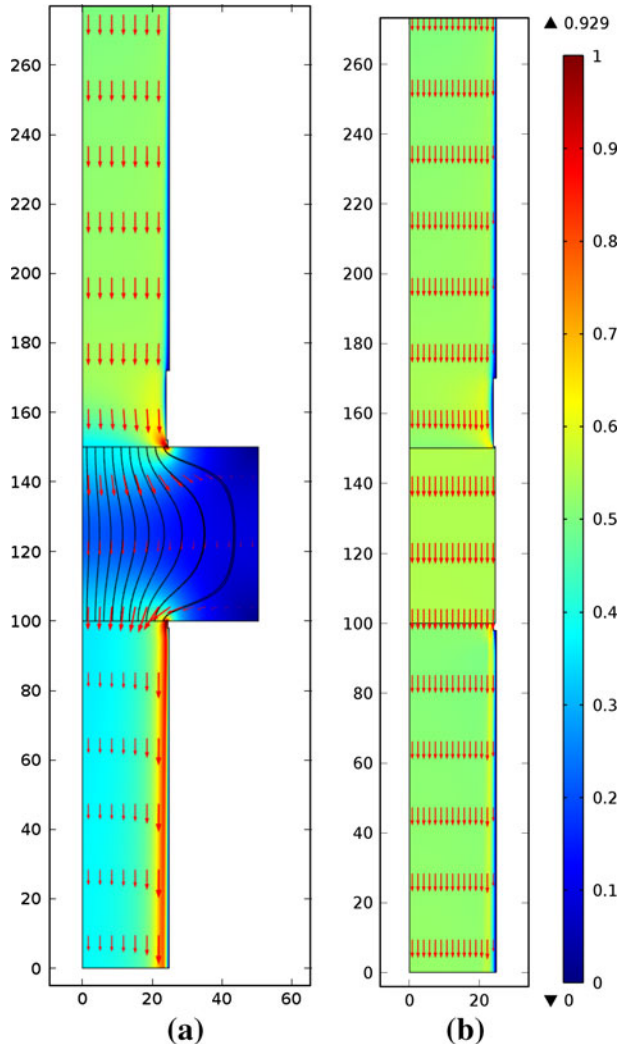

Fig. 12—Comparison of calculated flow fields for 50 PPI filters for the 101-mm "expanding flow field" (a) and 49-mm "straight through" (b) designs, both for 0.5 m/s uniform inlet velocity, and 280 K (7 °C) water temperature, shown with a common 0–1 m/s color scale. Pressure gradients of 501.1 and 1612.4 kPa/m were calculated for these two cases with the "short" inlet k_1 and k_2 parameters as shown in Table V.

Table V. Forchheimer Empirical Coefficients for Eq. [1]

| Filter Type (PPI)	Actual Filter Diameter (m)	Filter Thickness L (m)	Water Temperature (K)	Water Density ρ (kg/m^3)	Water Viscosity μ (Pa·s)	Eq. [1] Forchheimer k_1 (m^2)	Eq. [1] Forchheimer k_2 (m)	Inlet Length (m)
30	48.7	50.7	281.4	999.9	1.330E−03	5.08E−08	5.46E−04	1.0
30	101	50.7	280.2	999.9	1.374E−03	5.57E−08	5.25E−04	1.0
40	101	47.7	279.1	999.9	1.422E−03	3.10E−08	3.38E−04	1.0
50	49.2	49.6	280.1	999.9	1.378E−03	1.57E−08	1.66E−04	1.0
50	101	49.6	278.9	999.9	1.426E−03	1.71E−08	1.69E−04	1.0
50	101	49.6	280.0	999.9	1.382E−03	1.52E−08	1.71E−04	3.0
80	49.1	50.3	279.3	999.9	1.413E−03	6.52E−09	1.15E−04	1.0
80	101	50.3	280.8	999.9	1.351E−03	5.44E−09	9.96E−05	1.0
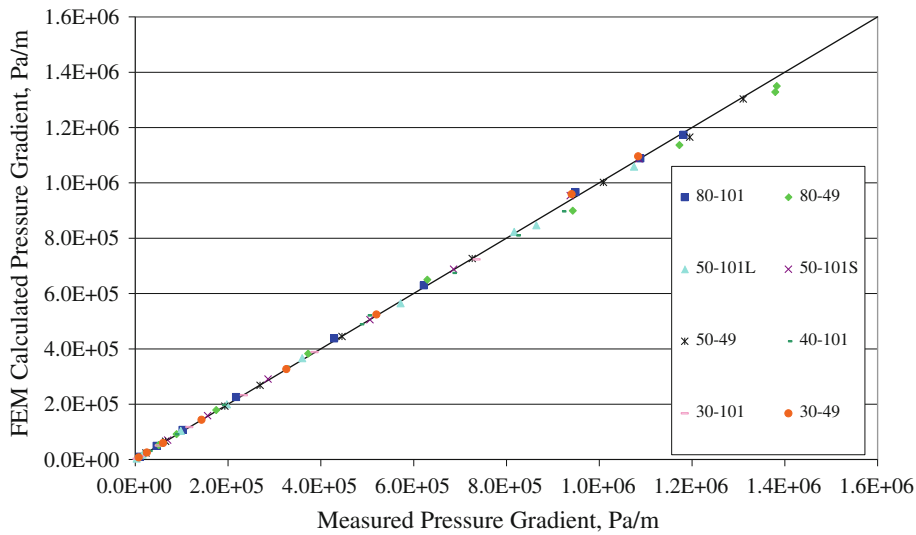
Fig. 13—FEM CFD results for 30 through 80 PPI filters of 101- and 49-mm nominal filter diameters, L = "long" (3 m) and S = "short" (1 m) inlet lengths, compared against the experimental pressure gradients (Pa/m).
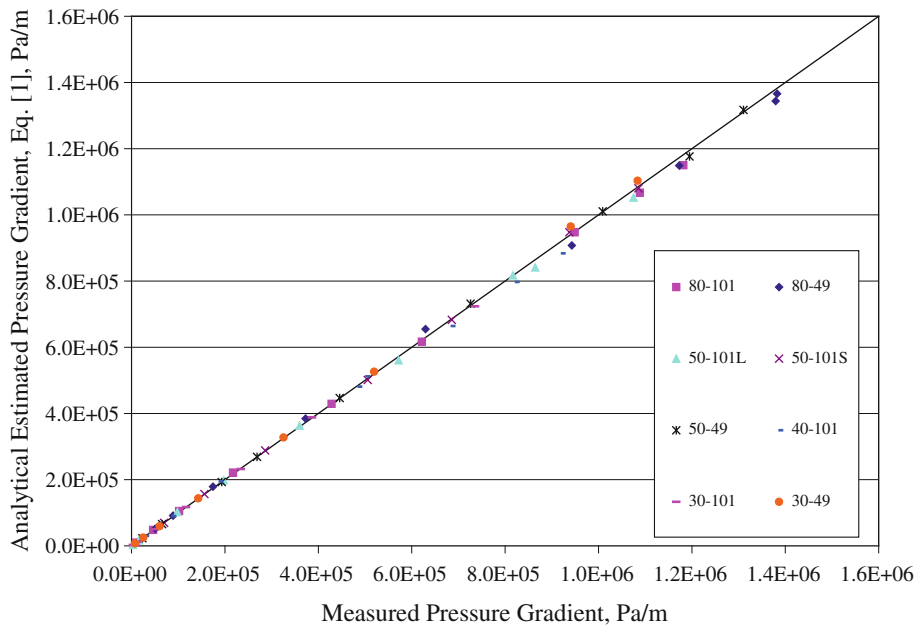

Fig. 14—Eq. [1] results for 30 through 80 PPI filters of 101- and 49-mm nominal filter diameters, L = "long" (3 m) and S = "short" (1 m) inlet lengths, compared with the experimental pressure gradients (Pa/m).

shown in Figure 17 for experiments conducted using the 80 PPI, 49-mm diameter filter.

The final experimental design used water-swollen cellulose and silicone to provide a very low permeability seal, which was not subject to physical removal at pressures of up to 0.8 bar. This was verified both visually and by repeated measurements over the whole pressure range with test filters. Results for the 80 PPI filter using this final procedure, are also presented in Figure 17. It is worth noting that all deviations in the experiments resulted in lower measured pressure gradients, *i.e.*, the highest measured pressure drop and the

lowest permeability value for a given filter are most probably the correct values.

Recently, Innocentini *et al.*[33] discussed the impact of bypassing and flow field expansion on measured pressure drops in metal foam. Examination of the change in pressure drop with filter thickness indicated that wall bypassing reduced the pressure drop and that the measured pressure drop did not increase linearly with larger thickness. It must therefore be assumed that the equipment was operating partially as an "annular orifice" along the wall. The flow field expansion in Innocentini's alternate apparatus design was not
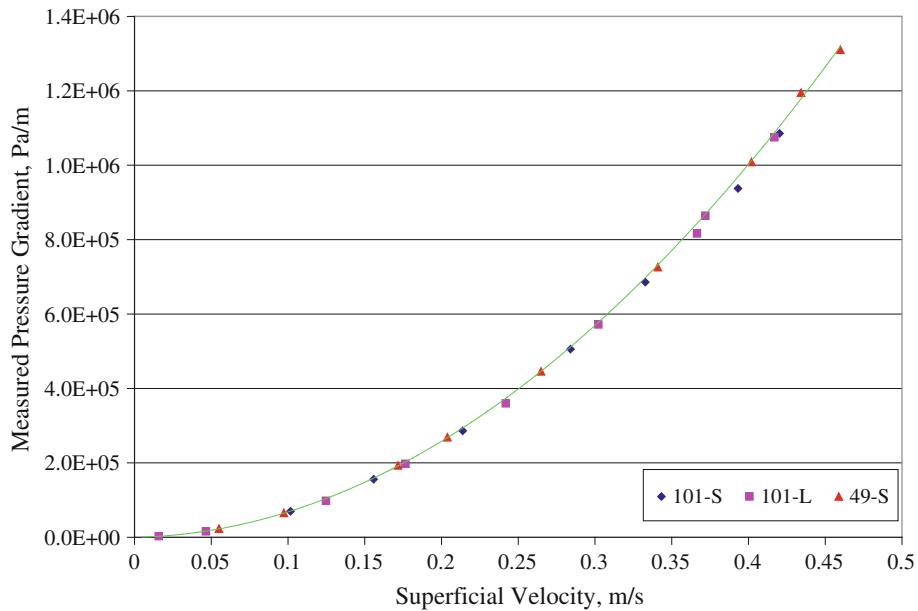
Fig. 15—Comparison between the L = "long" (3 m) and S = "short" (1 m) inlet length for the 101-mm and comparison with the 49-mm diameter filter results. Velocities are calculated using an "effective" flow diameter of 66.1 mm, determined by FEM/CFD for the 101-mm diameter filters.
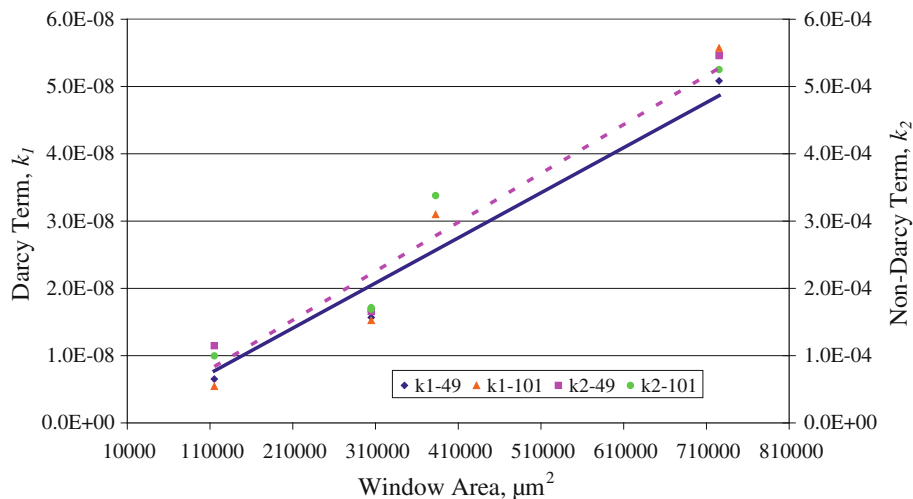

Fig. 16—Correlation of Darcy term, k_1 (m^2) and Non-Darcy term, k_2 (m) with window area $\frac{\pi d_w^2}{4}$. k_1 is correlated by the solid line and k_2 by the dotted line.

analyzed using CFD, and in both cases, no sealing was indicated at the walls.[33]

C. Correlation of Results, and Comparison with Dietrich and Ergun

Extensive efforts have been made to correlate the obtained results and compare with previously published equations. Of the previously published equations, only the equation of Dietrich, Eq. [8], was found to adequately describe the data. This comparison is made for the 30, 50, and 80 PPI, "straight through" 49-mm results shown in Figure 18. Agreement is considered as

adequate being typically within ±50 pct (except at low velocity), i.e., it achieves a similar accuracy for foams, as the original Ergun equation achieves for packed beds.

Other equations were found to underestimate dramatically the measured pressure drops obtained using the final and "well-sealed" experimental procedure. Most previously published equations did describe the obtained results for the "straight through" experiments in the absence of a wall seal or the "expanding flow field" results in the absence of area correction. No firm conclusions can be drawn from these facts, as details on the sealing arrangements and analysis techniques used in previous studies are generally lacking.
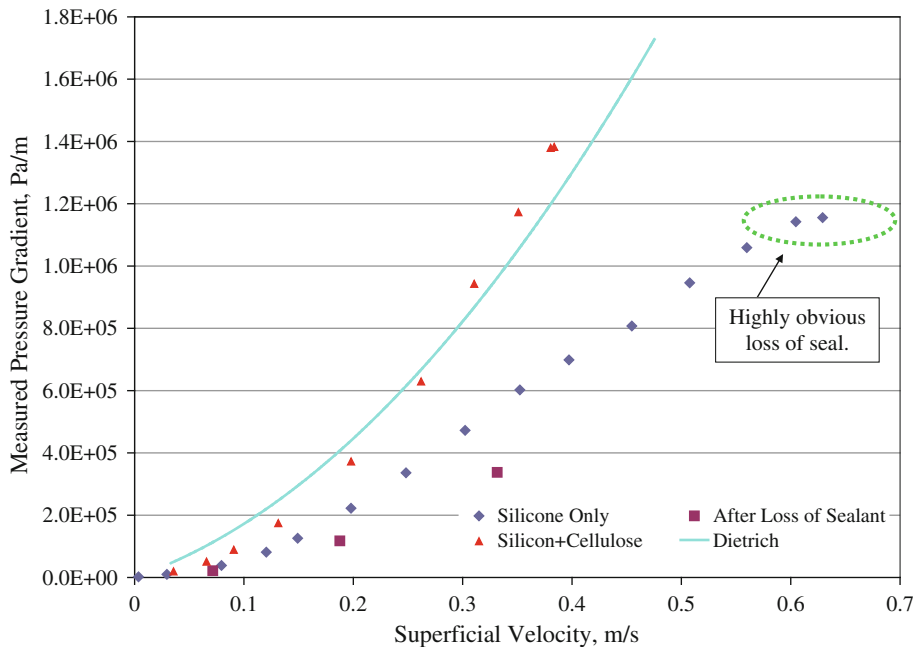
Fig. 17—Impact of sealing method and loss of seal on measured pressure gradients for 49-mm diameter "straight through" design using an 80 PPI filter element as a function of water superficial velocity. Comparison is made with Dietrich's equation [8].[10,11]
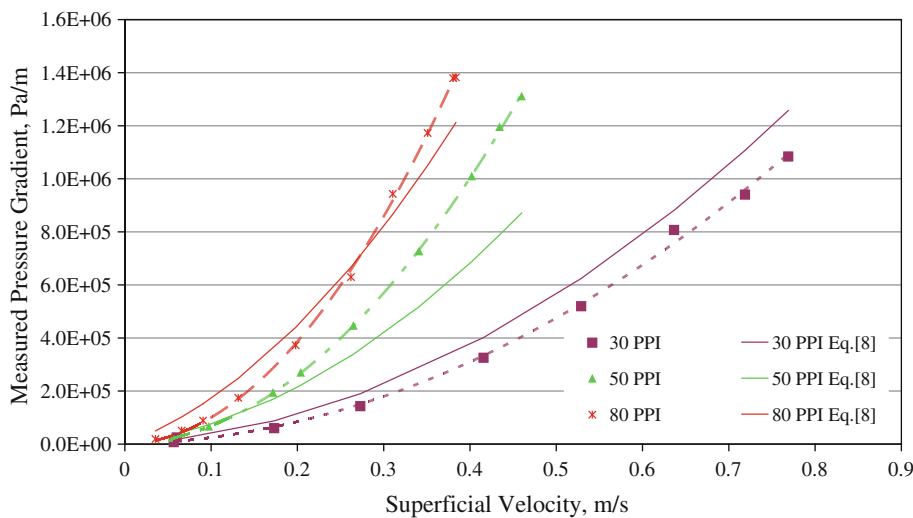

Fig. 18—Comparison between Dietrich's Eq. [8][10,11] and measured data for the 49-mm diameter "straight through" 30, 50, and 80 PPI filters' measured data. Experimental data are plotted with dotted lines and symbols, Dietrich's predictions are plotted as solid lines.

The best empirical correlation obtained was a slightly modified version of Ergun's equation.[7]

$$\frac{\Delta P}{L} = 8.385 \left(150 \frac{(1-\varepsilon)^2}{\varepsilon^3} \frac{\mu V}{D_w^2} + 1.75 \frac{(1-\varepsilon)}{\varepsilon^3} \frac{\rho V^2}{D_w} \right), R^2 = 0.95$$ [22]

Equation [22] is plotted in Figure 19, along with the + 30 and −30 pct lines.

Equation [22] is equivalent to using 23.4 and 2.00 (based on an average $\varepsilon = 0.88$), as the empirical

constants, instead of the values 110 and 1.45 in Dietrich's Eq. [8] or the Ergun equivalent values of 66.7 and 1.17 from Eq. [7]:

$$\frac{\Delta P}{L} = 23.4 \frac{\mu V_s}{\varepsilon d_h^2} + 2.00 \frac{\rho V_s^2}{\varepsilon^2 d_h}$$ [23]

Applying Eq. [23] to the obtained data indicates a significant reduction in error compared with the original Eq. [8], particularly at low velocity and pressure and an overall reduction in average error from ~40 pct to

$$8.385\left(150\frac{(1-\varepsilon)^2}{\varepsilon^3}\frac{\mu V}{D_w^2}+1.75\frac{(1-\varepsilon)}{\varepsilon^3}\frac{\rho V^2}{D_w}\right)$$
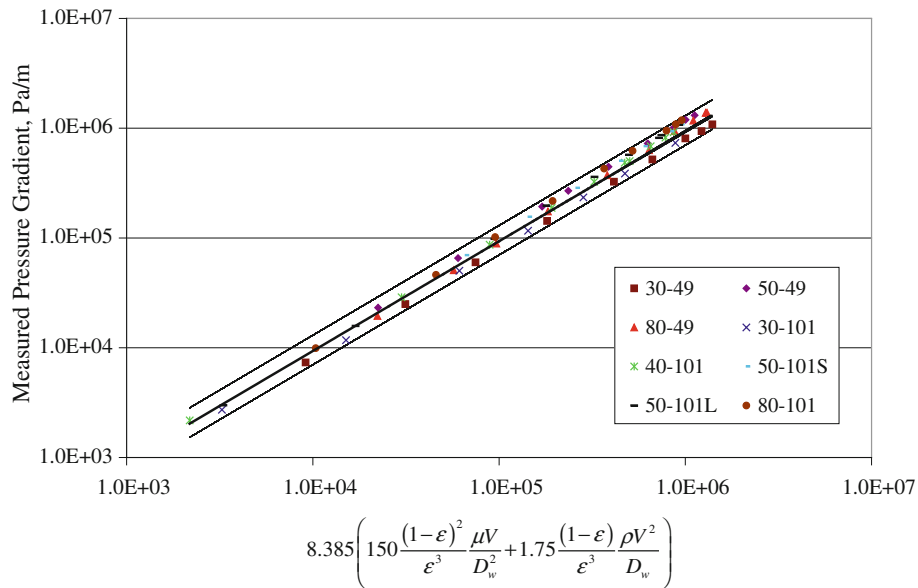
Fig. 19—Overall correlation Eq. [22], comparison with the measured pressure gradients ranging from 30 to 80 PPI filter elements. 49-mm diameter measurements were not available for the 40 PPI filters, as the filter exhibited poor mechanical properties and disintegrated on cutting. The upper and lower lines in the figure indicate a range of ±30 pct.
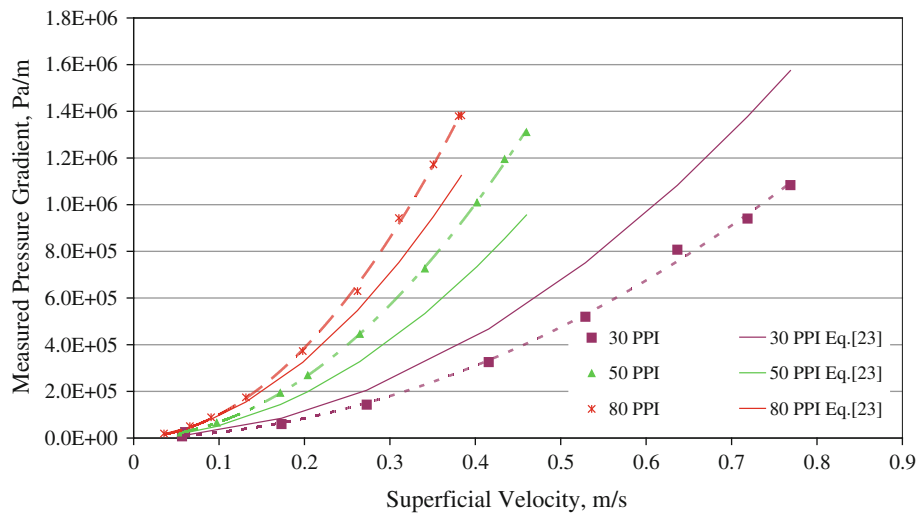

Fig. 20—Comparison of the modified Dietrich Eq. [23] with experimental data for the 49-mm diameter "straight through" experimental results from the 30, 50, and 80 PPI filters.

~30 pct. Equation [23] is plotted against the 30, 50, and 80 PPI, "straight through" 49-mm results in Figure 20.

Attempts were made to use cell diameter, d_c, strut diameter, d_s, and tortuosity, τ, in various correlations; however, no improvement could be made over the accuracy of Eqs. [23], [22], or [8].

D. Comments Regarding CFD Modeling

The CFD models presented here are discussed in more detail elsewhere.[34] Some pertinent points to achieving adequate agreement between FEM, analytic models and measured values are as follows:

(a) Iteration between high-quality measurements and FEM to ensure validity of assumptions and accuracy of final models.

(b) Correct and validated boundary conditions, e.g., no-slip walls, contiguous velocity fields between liquid and porous media domains, and the inlet velocity profile.

(c) Use of the low Reynolds number k-ε, and Reynolds Averaged Navier–Stokes (RANS) model for turbulence ($k_0 = 0.005$ m^2/s^2 and $\varepsilon_0 = 0.005$ m^2/s^3), to adequately cover the difficult range of velocities in the inlet region.

(d) Use of dense meshes in regions of high velocity gradients (e.g., boundary mesh at the "no-slip" walls).

(e) Precise measurement and exact geometric reproduction of the actual apparatus.

It is important to note that if significant bypassing had occurred during these experiments, it would not have been possible to achieve agreement between the CFD model and the experimental data for the 49-mm filter design. The agreement between the CFD results and the 49-mm and, subsequently that between the 49-mm and the 101-mm designs, are taken as confirmation that the wall-sealing arrangements in fact were of negligible permeability.

VI. CONCLUSIONS

Pressure gradients in CFFs have been found to correlate against velocity with high precision at both low and high velocities, using the Forchheimer equation, Eq. [1]. Forchheimer first-order k_1 and second-order k_2 terms were both found to correlate directly with the measured mean window area for each filter type (30, 40, 50, and 80 PPI).

The obtained pressure drops in this study could be best estimated using the measured total porosity ε, the optically determined window size d_w, and either Dietrich's original equation, Eq. [8], a modified version of Dietrich's equation, Eq. [23], or a slightly modified Ergun equation [22].

Bypassing along the wall must be prevented if accurate permeabilities of CFFs are to be measured using water flow experiments.

If the diameter of the filter is larger than the diameter of the pipe, then CFD must be used to analyze the impact of the expansion of the flow field on the measured pressure drop, i.e., to determine the effective flow field diameter for use with Eq. [1].

Care must be taken while determining how results are mathematically correlated to prevent small percentage errors with the large pressure drops at high velocity from producing too much "noise" in the determination of first-order empirical coefficients for use with the Forchheimer equation, Eq. [1].

VII. FUTURE STUDY

Experiments should be conducted to elucidate the change of filter pressure drop with filter thickness. This would provide further validation that wall bypassing has been prevented by the current experimental procedures and/or determine the impact of bypassing on measured filter permeabilities.

Additional experiments should be conducted with filters produced from different suppliers and with other filter pore densities, to attempt to improve upon the Dietrich/modified Dietrich equations presented above.

Additional experiments could be conducted with a low range, from 0 to 0.1 bar pressure transducer, at low velocity (0 to 0.05 m/s), to study the Darcy and transitional regions in greater detail.

The conductivity of metals is best known and can be most easily measured at room temperature. It is recommended that for future tortuosity measurements, impregnate and then cool and solidify the sample. Solid samples can then be machined to precise tolerances, and inductive heating experiments can then be conducted at room temperature and low frequency to determine the tortuosity. Water cooling can even be applied to directly measure the quantity of heat produced and allow operation at steady-state thermal conditions, as has been applied elsewhere.[35]

APPENDIX

See Appendix Tables I and II.

Appendix Table I. Tortuosity Experimental Data and FEM Calculated Conductivity Ratios

Filter Type (PPI)	Average Metal Temperature (K)	Estimated Hot Metal Conductivity Using Eq. [14] (ohm m)$^{-1}$	Experimental Current (A)	Experimental Power (W)	FEM Estimate of Conductivity Ratio (σ_m/σ_f)
30	947	3.70E+06	716.9	1462	1.50
30	1000	3.58E+06	728.0	1469	1.51
30	1048	3.50E+06	517.7	764	1.42
30	995	3.60E+06	371.2	404	1.40
Room temperature final metal conductivity: 60.0 pct IACS, ±0.2 pct, 6 counts					1.46
40	940	3.34E+06	628.5	790	2.75
40	1026	3.09E+06	628.7	836	2.42
40	1033	3.17E+06	629.0	827	2.45
Room temperature final metal conductivity: 54.0 pct IACS, ±0.8 pct, 48 counts					2.54
Likely Fe or Si Al alloy contamination from melting crucible or metal skimming tool					
50	933	3.78E+06	728.3	1078	2.67
50	957	3.73E+06	727.8	1105	2.54
50	983	3.68E+06	728.0	1059	2.65
50	1021	3.60E+06	728.2	1053	2.61
50	1044	3.56E+06	729.2	1039	2.63
50	1052	3.54E+06	632.7	840	2.38
50	1044	3.56E+06	632.7	854	2.34
50	1032	3.58E+06	634.0	820	2.50
Room temperature final metal conductivity: 61.0 pct IACS, ±0.5 pct, 66 counts					2.54
80	948	3.68E+06	732.4	831	3.75
80	954	3.66E+06	732.9	832	3.74
80	963	3.65E+06	733.6	852	3.60
80	972	3.62E+06	733.4	814	3.80
80	979	3.61E+06	733.1	823	3.72
80	985	3.60E+06	733.1	823	3.71
80	991	3.59E+06	732.9	832	3.63
80	994	3.58E+06	732.9	817	3.72
80	997	3.58E+06	733.0	827	3.66
Room temperature final metal conductivity: 59.7 pct IACS, ±0.4 pct, 37 counts					3.70

Appendix Table II. Detailed Permeability Experimental Results

Filter Type (PPI)	Effective Filter Diameter (m)	Filter Thickness (m)	Water Temperature (K)	Water Density (kg/m³)	Water Viscosity (Pa s)	Excel 2003 Forchheimer k_1 (m²)	Excel 2003 Forchheimer k_2 (m)	Ergun Method Forchheimer k_1 (m²)	Ergun Method Forchheimer k_2 (m)	Method 3 Forchheimer k_1 (m²)	Method 3 Forchheimer k_2 (m)	Inlet Length (m)
30	48.7	50.7	281.4	999.9	1.330E–03	2.14E–08	5.83E–04	4.58E–08	5.48E–04	5.08E–08	5.46E–04	1.0
30	65.5	50.7	280.2	999.9	1.374E–03	2.46E–07	5.10E–04	7.19E–08	5.18E–04	5.57E–08	5.25E–04	1.0
40	66.0	47.7	279.1	999.9	1.422E–03	–2.03E–08	3.05E–04	1.09E–07	3.24E–04	3.10E–08	3.38E–04	1.0
50	49.2	49.6	280.1	999.9	1.378E–03	1.84E–08	1.65E–04	1.63E–08	1.65E–04	1.57E–08	1.66E–04	1.0
50	66.1	49.6	278.9	999.9	1.426E–03	1.63E–08	1.69E–04	1.24E–08	1.72E–04	1.71E–08	1.69E–04	1.0
50	66.1	49.6	280.0	999.9	1.382E–03	4.67E–08	1.64E–04	2.17E–08	1.67E–04	1.52E–08	1.71E–04	3.0
80	49.1	50.3	279.3	999.9	1.413E–03	1.90E–08	1.08E–04	8.68E–09	1.11E–04	6.52E–09	1.15E–04	1.0
80	66.5	50.3	280.8	999.9	1.351E–03	9.69E–09	9.45E–05	6.58E–09	9.68E–05	5.44E–09	9.96E–05	1.0

REFERENCES

1. M. J. Pryor: US Patent 3,893,917, 1975.
2. M.W. Kennedy, S. Akhtar, J.A. Bakken, and R.E. Aune: *Metall. Mater. Trans. B*, in press.
3. M.W. Kennedy, S. Akhtar, J.A. Bakken, and R.E. Aune: *Light Metals*, San Diego, CA, 27 February to 3 March, 2011, pp. 763–68.
4. Sivex® Application Guidelines, Jan-10-E4-565.
5. B. Hübschen, J. Krüger, J. Keegan, and W. Schneider, *Light Metals,* 2000, pp. 809–15.
6. P. Forchheimer: *Z. Ver. Deutsch. Ing*, 1901, vol. 45, pp. 1782–88.
7. S. Ergun: *Chem. Eng. Prog.*, 1952, vol. 48, pp. 89–94.
8. I. Macdonald, M. El-Sayed, K. Mow, and F. Dullien: *Ind. Eng. Chem. Fundam.*, 1979, vol. 18, pp. 199–208.
9. J. Richardson, Y. Peng, and D. Remue: *Appl. Catal. A*, 2000, vol. 204, pp. 19–32.
10. B. Dietrich, W. Schabel, M. Kind, and H. Martin: *Chem. Eng. Sci.*, 2009, vol. 64, pp. 3633–40.
11. B. Dietrich: *Chem. Eng. Sci.*, 2012, vol. 74, pp. 192–99.
12. S.A. Shakiba, R. Ebrahimi, and M. Shams: *J. Fluids Eng.*, 2011, vol. 133, pp. 111105-1–10.
13. M.W. Kennedy, R. Fritzsch, S. Akhtar, J.A. Bakken, and R.E. Aune: U.S. Provisional Patent Application 61/639,196, 2012.
14. J. Große, B. Dietrich, H. Martin, M. Kind, J. Vicente, and E.H. Hardy: *Chem. Eng. Technol.*, 2008, vol. 31, pp. 307–14.
15. B. Dietrich, G.I. Garrido, P. Habisreuther, N. Zarzalis, H. Martin, M. Kind, and B. Kraushaar-Czarnetzki: *Ind. Eng. Chem. Res.*, 2009, vol. 48, pp. 10395–401.
16. Copper Wire Tables Circular No. 31: US Bureau of Standards, 1913, pp. 1–76.
17. R. Fritzsch, M.W. Kennedy, S. Akhtar, J.A. Bakken, and R.E. Aune, *Electromagnetic Processing of Materials*, 23–25 October, Beijing, China, 2012, pp. 1–4.
18. P. Desai, H. James, and C. Ho: *J. Phys. Chem. Ref. Data*, 1984, vol. 13, pp. 1131–72.
19. M.W. Kennedy, S. Akhtar, J.A. Bakken, and R.E. Aune, *COMSOL Users Conference*, 26–28 October, Stuttgart, Germany, 2011, pp. 1–9.
20. M.W. Kennedy, S. Akhtar, J.A. Bakken, and R.E. Aune, *Light Metals*, Orlando, Florida, 3–7 March, 2012, pp. 269–75.
21. L.F. Moody: *Trans. ASME*, 1944, vol. 66, pp. 671–84.
22. W. Zhi-qing: *Appl. Math. Mecha.*, 1982, vol. 3, pp. 433–46.
23. F.M. White, *Fluid Mechanics*, 4th ed., McGraw Hill, Boston, 1999, pp 331–32.
24. N. Keegan, W. Schneider, and H. Krug, *Light Metals,* 1999, pp. 1031–41.
25. E. Moreira, M. Innocentini, and J. Coury: *J. Eur. Ceram. Soc.*, 2004, vol. 24, pp. 3209–18.
26. G. Diedericks and J.Du. Plessis: *Adv. Water Resour.*, 1996, vol. 19, pp. 225–39.
27. S. Ergun and A.A. Orning: *Ind. Eng. Chem.*, 1949, vol. 41, pp. 1179–84.
28. T. Lu, H. Stone, and M. Ashby: *Acta Mater.*, 1998, vol. 46, pp. 3619–35.
29. M. Lacroix, P. Nguyen, D. Schweich, C.Pham. Huu, S. Savin-Poncet, and D. Edouard: *Chem. Eng. Sci.*, 2007, vol. 62, pp. 3259–67.
30. T.T. Huu, M. Lacroix, C.Pham. Huu, D. Schweich, and D. Edouard: *Chem. Eng. Sci.*, 2009, vol. 64, pp. 5131–42.
31. M.V. Twigg and J.T. Richardson: *Ind. Eng. Chem. Res.*, 2007, vol. 46, pp. 4166–77.
32. A. Inayat, J. Schwerdtfeger, H. Freund, C. Körner, R.F. Singer, and W. Schwieger, *Chem. Eng. Sci.*, 2011, vol. 66 (12), pp. 2758–63.
33. M.D.M. Innocentini, L. Lefebvre, R. Meloni, and E. Baril: *J. Porous Mater.*, 2010, vol. 17, pp. 491–99.
34. M.W. Kennedy, R. Fritzsch, J.A. Bakken, and R.E. Aune: *Presented at COMSOL® User's Conference*, Milan, Italy, 10–12 October, 2012, pp. 1–7.
35. M.W. Kennedy, S. Akhtar, J.A. Bakken, and R.E. Aune, *3rd International Symposium on High Temperature Processing*, Orlando, Florida, 3–7 March, 2012, pp. 373–82.